4 Measured Irreversibilities of Incompressible Flows

4.1 INTRODUCTION

This chapter presents experimental methods to enable measurements leading to the spatial distribution of entropy production within a flow field. Measured entropy production provides a valuable diagnostic tool from which economic impact of exergy losses (losses of work potential) could be determined. Rosen and Dincer (2003) have developed exergoeconomic methods to assess economic impact of exergy losses in various industrial systems, such as power plants operating on various fuels and thermal energy storage systems (Dincer and Rosen, 2000). Linking exergy losses directly with financial losses is a powerful tool for driving changes within energy systems to reduce losses of useful work, which would be otherwise underestimated without understanding their economic impact on system viability.

In this chapter, the experimental techniques will focus on the combined use of particle image velocimetry (PIV) and planar laser-induced fluorescence (PLIF). PIV measures the spatial distribution of fluid velocity, whereas PLIF is used to acquire temperature data in a flow field. The combined PIV-PLIF method offers certain advantages over standard methods of anemometry for experimental studies of entropy production. Previous methods, limited by single-point measurement techniques, can only measure single-point entropy production or averaged entropy production over a finite volume. On the other hand, PIV-PLIF methods provide whole-field methods, while allowing nonintrusive and time-varying measurements of the instantaneous velocity and temperature distributions within a flow field. This chapter presents a detailed description of methods to collect physical data on the detailed structure of entropy production throughout a flow field. The PIV and PLIF techniques provide multipoint instantaneous data, so they enable measured data for local variations of the entropy production rates. In this chapter, the experimental techniques will give whole-field measurements of entropy production with these nonintrusive, optical methods.

4.2 EXPERIMENTAL TECHNIQUES OF IRREVERSIBILITY MEASUREMENT

4.2.1 Velocity Field Measurement

Whole-field velocity data are needed before the local entropy production rates can be determined. PIV is a widely used experimental method based on light scattering by small particles in a flow fluid, which are illuminated by two laser light pulses at very short intervals. The scattered light has the same frequency as incident laser light at

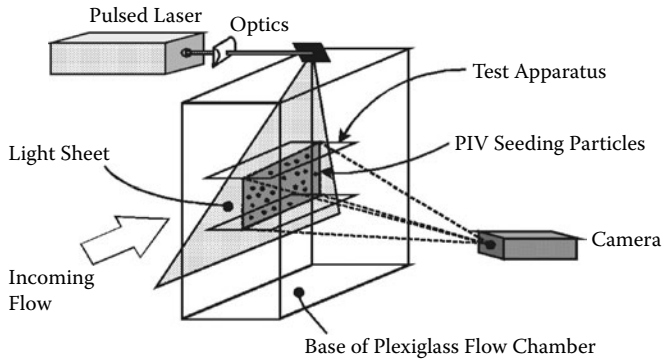

FIGURE 4.1 Schematic of particle image velocimetry configuration.

low wavelengths. In contrast, laser-induced fluorescence (LIF) does not result from a scattering process, but rather an absorption and wavelength conversion process. The light emitted by molecules and atoms in a de-excitation process, induced by absorption of a photon of higher energy (from a laser source), is red-shifted to longer wavelengths. These combined features of PIV-PLIF allow synchronization of measurement techniques for both thermal and friction irreversibility measurements, without duplication of hardware.

The optical configuration for a typical PIV-PLIF setup consists of a light source, light sheet optics, fluorescent dye for PLIF, processor with software, and tracer particles for PIV and CCD or CMOS cameras (see Figure 4.1). In two-dimensional PIV, the pulsed laser illuminates a planar cross section in the center of the flow region of interest, parallel to the flow and perpendicular to the camera. The camera captures the image of the illuminated particles in successive frames at each instant when the light sheet is pulsed. The two successive images are processed, subdivided into small interrogation regions, and matched based on a correlation analysis to determine the displacement of a group of particles, elapsed time, and the local fluid velocity. Denoting M as the magnification of the camera, the velocity is given by a first-order estimate as follows:

$$\vec{U} = \frac{M\Delta\vec{s}}{\Delta t} \tag{4.1}$$

where $\Delta\vec{s}$ is a displacement vector in the image plane and Δt is the pulse time interval (Willert and Gharib, 1991).

Interrogation analysis is an important element of the PIV technique. The spatial velocity distribution is obtained over a regular grid of small subregions using statistical methods. The recorded image frame is divided into small areas, called interrogation areas. Correlation-based techniques are used within each interrogation region to produce a vector representing the average particle displacement. Autocorrelation and cross-correlation techniques are used for high particle density image analysis, whereas other methods like particle tracking and particle pairing are limited to relatively

low-density images. A high-density image arises when the number of particles is between 7 and 10 image pairs per interrogation area. In autocorrelation, an interrogation area is correlated with itself. In this section, the analysis will correlate an interrogation area with a second area, which is offset in the mean flow direction. The cross-correlation employed within each interrogation area allows a precise determination of the direction of displacement to give instantaneous values of both components of fluid velocity in two dimensions. Westerweel (1997) and Adrian (1991) provide additional details regarding interrogation analysis in PIV methods.

The PIV resolution becomes more important for high Reynolds number experiments that attempt to resolve small-scale variations embedded with in a large-scale motion. Such scenarios exist in turbulence measurements and cases where small-scale flow structures around large objects must be resolved. Two key velocity resolution issues arise in these types of problems (FlowMap, 1998), namely, (1) the dynamic velocity range, which relates to the ability to resolve very small velocity displacements between particle image pairs, and (2) the dynamic spatial range, which relates to the size of the smallest velocity structure that can be resolved in the flow field.

The dynamic spatial range is defined as the field of view in the object space, divided by the smallest resolvable spatial variation (Adrian, 1997). This range coincides with the number of independent vectors obtained from the interrogation analysis (without overlapping). The smallest-length scale that can be resolved is given by

$$\lambda_{min} = \frac{N_I d_p}{M} \tag{4.2}$$

where L_o is the physical dimension of the field of view in the x direction, L_I is the corresponding pixel dimension of the camera, N is the number of interrogation areas, and d_p is the pixel pitch of the CCD array.

For a 32×32 pixel interrogation area, each flow field is resolved to a factor of approximately 32 in the field of view. This dynamic spatial range would be low for turbulence measurements. A decrease in the resolved length scale, λ_{min}, would require the reduction of the view area size to a fixed number of interrogation cells. Higher resolution can be achieved by a higher magnification of the measurement area, such as extension rings between the lens and the camera. However, higher magnification of the image may lead to higher velocity bias errors. Better modifications include a higher resolution CCD (higher number of pixels) or higher format recording media with physical dimensions on the order of 1 cm. The dynamic range is the ratio of the maximum velocity to the minimum velocity resolvable by a particular PIV system. The minimum resolvable velocity occurs in the order of the root mean square (rms) error, when determining the displacement of the particle image.

4.2.2 Temperature Field Measurement

Spatial variations of temperature within the flow field are needed to determine the thermal irreversibilities of entropy production, and they can be determined from PLIF. In PLIF, molecules and atoms of a fluorescent dye are excited to a higher electronic energy state, by pulsed laser absorption and fluorescence. The local fluorescence intensity, I, varies with intensity of excitation light, I_e; concentration of the

fluorescent dye, C; quantum efficiency as a function of temperature, ϕ; and the molar absorptivity, ε, as follows:

$$I = fI_e \varepsilon C \phi(T) \tag{4.3}$$

where f is a factor corresponding to the optical setup. For a known concentration and excitation energy, the quantum energy decreases at higher temperatures. This dependence constitutes the basis for PLIF temperature measurements. The temperature is determined as follows:

$$T - T_{ref} = \frac{\Delta I}{fI_e \varepsilon C \Delta \phi} \tag{4.4}$$

Thus, quantitative analysis is based on temperature calibration images that correlate the variation of intensity of the image with the local temperature and laser energy.

The first step in the PLIF calibration procedure is to find the optimum concentration resulting in the maximum temperature resolution with low absorption phenomena. The corresponding absorption, A, can be calculated from

$$A = e^{-l\eta_{Rhod}C} \tag{4.5}$$

where η_{Rhod} is the extinction coefficient of Rhodamine B in water and l is the optical path length. The experimental procedure would involve running a series of trials at a fixed energy level to determine the optimum concentration at which the temperature resolution is maximum, while maintaining linearity between the gray level and temperature. The measurement precision of a particular concentration value is indicated by the slope of the curve obtained in the preliminary experiment. Typically, the temperature resolution approaches an asymptotic minimum at an optimum concentration, and then it increases thereafter.

Signal processing consists of a final translation of the recorded images to temperatures via the calibration maps. The final calibration relates the response of every pixel of the CCD camera to varying temperature, laser energy levels, and concentration. The temperature at discrete locations in an actual measurement region is determined from

$$T - T_{ref} = \frac{I - I_{ref}}{\beta} \tag{4.6}$$

where I_{ref} is the intensity of the fluorescent signal at the reference temperature, T_{ref}. The denominator is statistically determined during calibration. The wavelength of the fluorescence emitted from PLIF is longer than the wavelength of the reflected laser light, thereby making simultaneous measurements of both velocity and temperature possible. An optical filter can be attached to the front of the camera for the fluorescent image to cut off reflected light from the PIV particles.

The camera and image capturing systems detect particle images and fluorescent images successively at two different instants. Postprocessing of the velocity and temperature measurements will allow the estimation of entropy production. In addition, the temperatures can be resampled with spatial resolution of the PIV vectors, ensuring maximum correlation between the thermal and friction irreversibilities. Experimental correlations between velocity and temperature will provide useful data for turbulent entropy transport modeling in upcoming chapters.

4.2.3 Postprocessing for Entropy Production Measurement

Unlike velocity or temperature, the measurement of entropy cannot be performed directly. But the entropy production equation can be used in an indirect way to characterize the flow irreversibility. The measured velocities and temperatures are extracted over a discrete grid in the PIV software. The velocity and temperature fluids at grid position (i,j) are denoted by $u(i,j)$, $v(i,j)$, and $T(i,j)$, respectively. From Section 3.2, a positive definite expression for entropy production rate was derived in terms of a sum of squared terms representing the frictional irreversibility (viscous dissipation) and thermal irreversibility (due to heat transfer). Discretizing that result for two-dimensional flows yields the following expression for entropy production in terms of measured velocity and temperature gradients, centered about the point (i,j):

$$\begin{aligned}\dot{P}_s = {} & \frac{k}{T(i,j)^2}\left[\frac{T(i+1,j)-T(i-1,j)}{\Delta x}\right]^2 + \frac{k}{T(i,j)^2}\left[\frac{T(i,j+1)-T(i,j-1)}{\Delta y}\right]^2 \\ & + \frac{\mu}{T(i,j)}\left[\frac{u(i,j+1)-u(i,j-1)}{\Delta y} + \frac{v(i+1,j)-v(i-1,j)}{\Delta x}\right]^2 \\ & + 2\frac{\mu}{T(i,j)}\left[\left(\frac{u(i+1,j)-u(i-1,j)}{\Delta x}\right)^2 + \left(\frac{v(i,j+1)-v(i,j-1)}{\Delta y}\right)^2\right]\end{aligned} \tag{4.7}$$

where Δx and Δy refer to the grid spacing in the x and y directions.

When calculating the previous derivatives of velocity, errors can occur as follows: (1) bias error associated with the displacement measurement, and (2) a propagated uncertainty due to spatial differentiation of the velocity field. For a smaller grid size, the bias error decreases. The bias error associated with the fast Fourier transform-based cross-correlation algorithm in commercial PIV software can been minimized by a subpixel resolution of the PIV images. The entropy production algorithm contains multiple products of velocity derivatives. Hence, it is imperative to minimize the error associated with the determination of spatial derivatives. Two approaches can be taken in this regard. A twice-differentiable empirical function could be fitted to the data. The spatial derivative is then obtained directly through the differential of the empirical function. This approach requires an elaborate, often

difficult, interpolation routine for multidimensional output of PIV. Another approach is a local piecewise smoothing of the experimental data followed by the application of forward differences, central differences, or a Richardson central difference scheme over an adaptive window to calculate the derivatives.

Smoothing or filtering of experimental data reduces the noise in terms of experimental scatter, and it performs a least-squares approximation through a path that minimizes error for all data points in the field. In commercial PIV software, an average filter can usually be implemented in the form of a top-hat Gaussian filter with uniform weighting. The size of vectors in the neighborhood of a position (i,j) is specified by odd numbers, m and n. The filter calculates an average of vectors in a rectangular domain of size $m \times n$ surrounding a vector. The average value is substituted for all entries in the initial matrix. The average can then be calculated by the following formula:

$$\overline{u}(x,y) = \frac{1}{mn} \sum_{i=x-\frac{n-1}{2}}^{x+\frac{n-1}{2}} \sum_{j=y-\frac{n-1}{2}}^{y+\frac{n-1}{2}} u(i,j) \tag{4.8}$$

In addition to the average filter, a spline fit based on a second-order polynomial least-squares algorithm can also be used for data smoothing. Smoothing algorithms mitigate against error in the calculation of derivatives and resulting entropy production. They provide better approximations to an actual flow loss distribution. The interpolation of smooth curves or surfaces should be limited to flow structures present in the raw data from which they were obtained.

4.3 CASE STUDY OF MAGNETIC STIRRING TANK DESIGN

This section applies the previous techniques to a case study involving measured entropy production of fluid mixing induced by a magnetic stirrer in a cuvette cube. In this case study, a PIV camera views a magnetic stirrer commonly used in chemical processing laboratories (see Figure 4.2). The rotational speed of the stirrer is

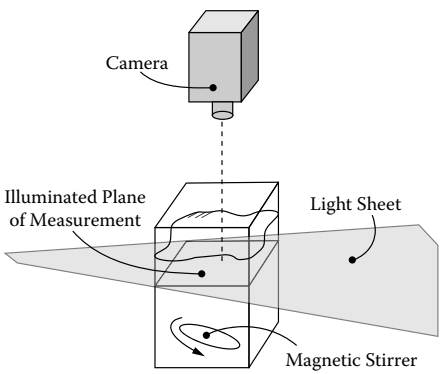

FIGURE 4.2 Schematic of magnetic stirrer.

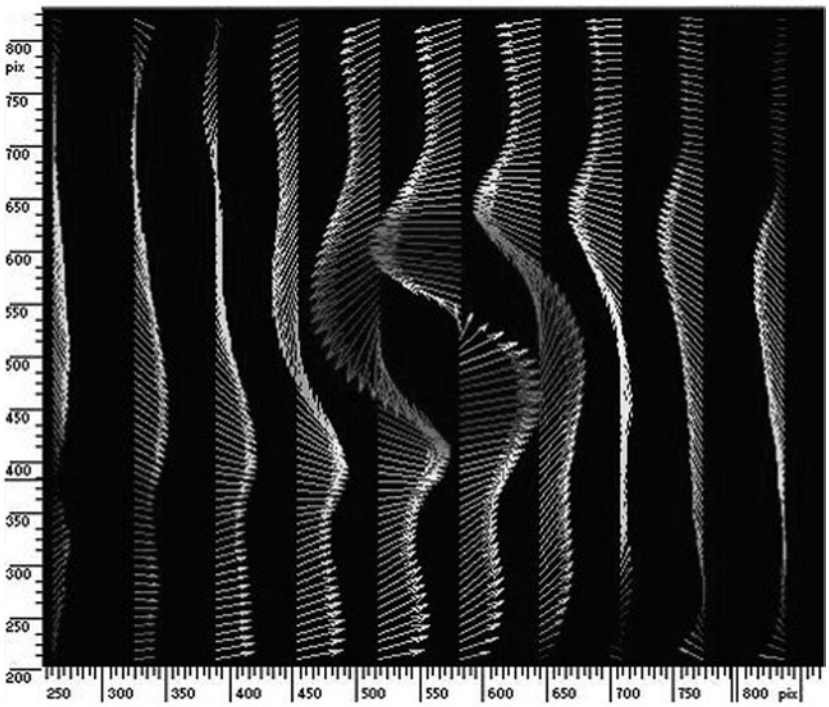

FIGURE 4.3 Measured velocity field.

90 r/min, which allows the camera, running at 30 Hz, to resolve each rotation with 20 image frames. Other problem parameters are summarized as follows:

- Cube side length: 60 mm
- Camera: 30 Hz
- Laser: Double-pulsed Nd:YAG laser at 10 mJ per pulse
- Light sheet entering the cuvette that is approximately 5 mm below the free surface
- Seeding: 50-mm polyamide particles
- Background: Ambient light used to capture the magnet stirrer in the images

Using Dantec Flow Map software, Figure 4.3 illustrates the measured velocity field within the plane of the light sheet used to illuminate the particles. Based on this velocity field, entropy production rates are determined and plotted in Figure 4.4. The regions of high mixing yield the highest rates of entropy production. In this example, the practical application of a magnetic stirrer involves mixing of chemicals to provide uniform mixtures. As a result, uniformly distributed magnitudes of entropy production would be desired to maximize mixing, rather than minimal entropy production in other applications like fluid machinery or power generation. Based on the

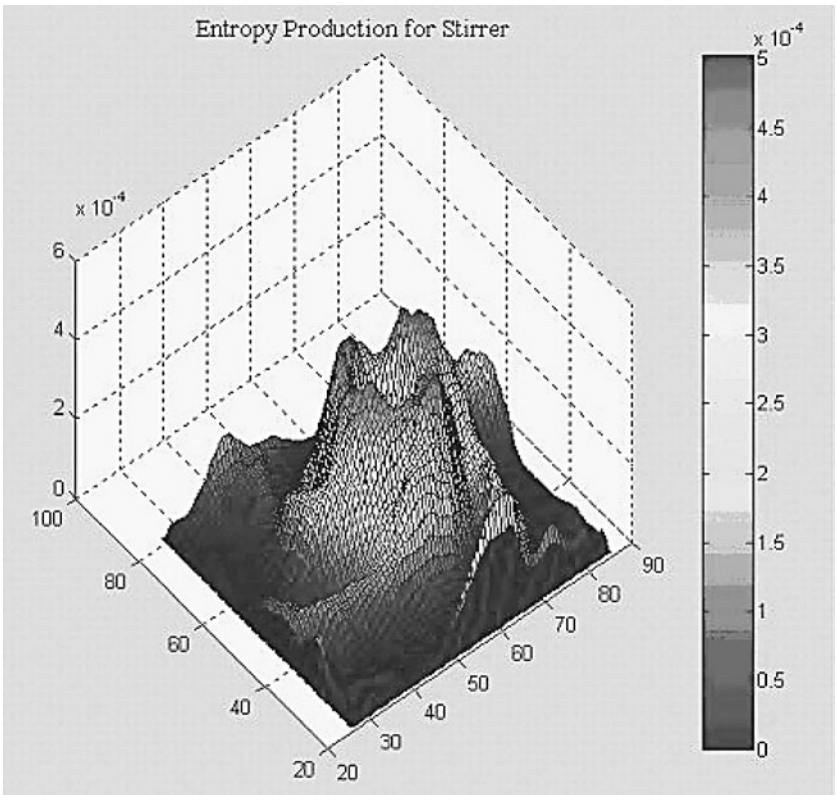

FIGURE 4.4 Surface profiles of entropy production.

measured entropy production rates, the impeller could be redesigned to extend the diffusive effects induced by mixing.

By summing the local entropy production measurements, the results provide a useful basis from which the energy efficiency of fluids engineering devices can be effectively characterized. Using the First Law of Thermodynamics, the thermal efficiency of a heat exchanger is defined differently from a water heater's efficiency, and still different from a diffuser's efficiency (in terms of pressure), and so on. Due to such inconsistencies, difficulty arises when trying to establish a standard way of identifying a device's energy wastefulness. Unlike methods based on the First Law, local or summed entropy production rates can provide a single, measurable quantity that is directly related to the efficiency of any energy-consuming or energy-producing device. The magnetic stirrer example in this section represents a single application where entropy production measurements can provide useful insight for design purposes. The practical utility of the method can be extended to numerous other applications, such as aerospace, automotive, power generation, turbomachinery, sprays, combustion, indoor ventilation, processing industries, and others.

4.4 CASE STUDY OF NATURAL CONVECTION IN CAVITIES

In this second case study, the measurement technique will be applied to natural convection in an enclosure. Free convection in enclosures occurs in various practical applications. Some examples include cooling of microelectronic assemblies, heat transfer between panes of glass in double-pane windows, solar collectors, and gas-filled cavities surrounding a nuclear reactor core. Although the physical processes of free convection have been widely documented in the literature, fewer studies have considered the related significance of entropy and the Second Low. For example, convective cooling within a microelectronic assembly entails free convection, whereas pressure losses occur with forced convection of air past internal components. In this instance, each unit of entropy produced leads to a corresponding unit of heat flow which is desired to be removed, but is not removed due to entropy production. This entropy production leads to pressure losses when kinetic energy is dissipated to internal energy, which works against the desired objective of component cooling.

Consider two-dimensional free convection within a square enclosure. The experimental setup involves PLIF for measuring temperatures within the test cell, as well as PIV for velocity measurements. An experimental study was conducted by Adeyinka and Naterer (2005) to measure entropy production in a 39×29-mm test cell. The cell depth of 59 mm was designed to minimize three-dimensional variations of thermal and flow fields along the plane of symmetry. Values of temperature at discrete locations in the measurement domain were obtained from the method of PLIF. In the commercial PLIF software, statistical averages are available to establish whole-field statistics of the LIF data. Further details regarding the experimental setup are described by Adeyinka and Naterer (2005).

The cavity is illuminated from above at the vertical plane of symmetry by an Nd:YAG pulsed laser. A CCD camera captures the sequence of image maps. The temperatures are recorded after their steady-state conditions are reached in both velocity and temperature fields. The Rayleigh number is controlled by adjusting fluid temperatures into the aluminum heat exchanger side walls. The PIV images are postprocessed by a fast Fourier transform based on a cross-correlation scheme in the Dantec Flow Map software. The PLIF images are resampled by a calibration map with a spatial resolution corresponding to the velocity map. As discussed in previous sections, the measured velocity vectors are displayed by the PIV software over a discrete grid. Using the velocity measurements and PLIF temperature measurements, the conversion algorithm for determining entropy production is then applied.

The PLIF measurements are used for temperatures in the expression for entropy production in Equation 4.7. For this buoyancy-driven problem, the temperature field varies spatially, thereby affecting the frictional entropy production in Equation 4.7. The nonintrusive method of PIV is used for whole-field measurements of velocity, which are then postprocessed by spatial differencing to yield local rates of entropy generation. In the experimental studies, the working fluid was water ($Pr = 8.06$). The left hot and right cold walls were maintained at 20 and 10 °C, respectively, thereby yielding a Rayleigh number of 5.35×10^6. The measured velocities indicate that a single clockwise recirculation cell developed with highest velocities near the side walls. The fluid velocities diminish rapidly at locations farther from

the wall. The velocities become too small for PIV vectors to be displayed in the central region of the cavity. The U-velocity results and V-velocity results along the vertical and horizontal midplanes, respectively, were also obtained. In each case, the velocities were nondimensionalized with respect to the maximum velocity, while the spatial coordinate was nondimensionalized with respect to the cavity width.

Close agreement between predicted and measured results was established. The measured velocity field is slightly skewed to the right side of the cavity, so some discrepancy between predicted and measured results was observed near the right wall. The numerical simulation assumes a perfectly insulated boundary on both horizontal walls of the cavity, which leads to complete symmetry without skewing of the velocity field. The experimental apparatus closely approaches this idealization, but any slight heat gains through the horizontal boundaries could potentially lead to asymmetry of the buoyancy-driven flow. Velocity measurements were obtained within 1 mm from the wall. In view of their importance in subsequent spatial differencing for entropy production at the wall, additional measurements were obtained by resolving the velocity field closer to the wall.

Surface plots of U-velocity values across the entire cavity were also obtained. The maximum horizontal velocity occurs near the top corner of the cold wall. Unlike fluid flow of air at $Pr = 0.71$, where the maximum U-velocity is closer to the hot wall in the top corner of the cavity, the predicted and measured results for water ($Pr = 8.06$) exhibit a maximum magnitude closer to the top corner of the cold wall. Buoyancy-induced acceleration of fluid up the hot wall leads to an adverse pressure gradient and velocity change, when the fluid is redirected horizontally near that corner. This momentum exchange involves a balance between fluid inertia and forces imparted by pressure, friction, and fluid buoyancy. The frictional resistance of the fluid along the wall increases, when the momentum diffusion rate exceeds the rate of heat diffusion ($Pr > 1$). This affects the overall momentum balance on the fluid, thereby altering pressure gradients near the top corners of the cavity and changing the trends of maximum fluid velocity for air ($Pr < 1$) and water ($Pr > 1$). Also, the distance of this maximum velocity point from the wall changes at different Prandtl numbers. Similarity solutions of free convection along a vertical wall confirm that the point of maximum velocity moves closer to the wall at higher Prandtl numbers (Naterer, 2002).

Postprocessing of the measured velocity results yields the spatial variation of entropy production throughout the cavity. The peak values occur at the vertical walls, corresponding to the locations of largest spatial gradients of velocity. Away from these points, entropy production decreases sharply to approximately zero close to the wall, which corresponds to the local maximum and zero gradient of V-velocity near the wall. Beyond this local maximum of velocity, entropy production increases to a local maximum and decreases back to nearly zero in the central region of the enclosure. The illustrated results have been normalized, with respect to a reference entropy production, P_s (*ref*), at the local maximum. The entropy production reaches a minimum value in the center of the cavity, where the stagnation point of the recirculation cell is observed.

Near-wall measurements of V-velocity and entropy production in the midregion of the cavity at the cold wall were also obtained. The measured maximum U and V

components of velocity were 0.611 and 1.69 mm/s, respectively, for this particular study. The predicted maximum U and V components of velocity are 0.632 and 1.89 mm/s, respectively. The close agreement between predicted and measured velocities near the wall are important because near-wall spatial gradients of velocity are needed for the entropy production calculations. Although PIV technology is limited by camera resolution and particle tracing of small-scale structures near the wall, the current experimental study successfully measured velocity and derived entropy production at very close proximity to the wall. A resolution of 0.2 mm was achieved in the wall region, which provided good near-wall accuracy that becomes particularly important for turbulent flows.

Measured oscillations of entropy production can be reduced through filtering of the velocity data. In the experimental study, a 3 × 3 average filter was used for smoothing of the raw velocity vectors, before calculating the entropy production. Previous PIV studies (Luff et al., 1999) have shown that filtering does not introduce additional error into the measured velocity, but it serves to mitigate uncertainty by averaging velocities at surrounding grid points. The measured results illustrate the benefit of filtering, particularly for the near-wall raw data points and removing random uncertainty in the measured velocity gradients. This measurement procedure for entropy production provides a useful diagnostic tool for identifying the local flow losses, so that energy conversion devices can be redesigned locally around regions of highest entropy production.

4.5 MEASUREMENT UNCERTAINTIES

4.5.1 Bias and Precision Errors

Uncertainty analysis involves systematic procedures of calculating error estimates for experimental data (Coleman and Steele, 1995). Measurement errors of entropy production arise from various sources. They can be broadly classified as bias errors and precision (or random) errors. Bias errors remain constant during a set of measurements. They are often estimated from calibration procedures or past experience. This section will assess both bias and precision errors in the entropy production measurements.

Elemental bias errors arise from calibration procedures or curve-fitting of calibrated data. Also, "fossilized" bias errors arise when measuring and tabulating thermophysical properties. Although such errors are usually less than ±1%, Coleman and Steele (1989) describe cases involving higher levels of fossilized bias errors. Moffat (1988) defines a "conceptual bias," which includes a residual uncertainty due to variability arising in the true definition of the measured variable. For example, if point measurements are used to approximate bulk temperatures at the inlet and exit of a duct, then the difference between these temperatures and the bulk mean temperature contributes to a conceptual bias error, because point measurements cannot fully capture the spatially averaged bulk value.

In contrast to bias errors, precision errors appear through scattering of measured data. Such errors are affected by the measurement system (i.e., repeatability, resolution) or spatial and temporal variations of the measured quantity. Also, the procedure itself may lead to precision errors arising from variations in operating conditions. If an error can be estimated statistically, then it is usually considered to

be a precision error. Otherwise, it is generally assumed to be a bias error. Anticipated precision errors are often used to guide experimental designs and procedures, in view of collecting data within a desired range of measurement uncertainty.

Gui et al. (2001) outline precision errors and other PIV measurement uncertainties in a towing tank experiment. Precision errors are reduced by increasing the number of measurement samples. Alekseeva and Navon (2002) found temperature uncertainties based on first- and second-order adjoint equations. An adjoint formulation of an inverse heat transfer problem leads to uncertainty indicators for the corresponding direct problem. Hessian maximum eigenvalues from the second-order adjoint equations can be used to evaluate the uncertainty indicators (Alekseeva and Navon, 2002). Pelletier et al. (2003) show how sensitivity equations provide key information regarding which parameters most affect the flow response. Measurement uncertainties of flow parameters depending on input data errors (such as initial and boundary conditions) can be effectively calculated with adjoint equations. Alekseeva and Navon (2003) use adjoint temperatures to calculate the transfer of uncertainties from such input data. Propagated uncertainties (Kline and McClintock, 1953) are often classified according to zero-order or higher-order uncertainties. In the former case, all parameters affecting the measurements are assumed to be fixed, except for the procedure of the experiment. Thus, data scattering arises from instrumentation resolution alone. In the latter case (higher-order uncertainty), control of the experimental operating conditions is considered, so factors such as time are included. The degree of variability of operating conditions can be expressed by the standard deviation.

Measurement uncertainties of primary variables (such as fluid velocity) with various experimental techniques have been widely reported previously, i.e., Kline (1985), Lassahn (1985), Moffat (1982), and others. Postprocessing of measured data, such as measured vorticity from postprocessed PIV data, entails additional uncertainties in the conversion algorithm. Conventional error indicators (AIAA Standard, 1995) can be extended to the scalar variable of entropy production. In this case, bias errors must be specifically correlated with sensitivity coefficients of the measured entropy production. Equation 4.7 expressed the measured entropy production as a postprocessed variable. Before assessing the experimental uncertainties in this method, the first step is assessing the uncertainties of measured velocities.

4.5.2 Velocity Field Uncertainties in Channel Flow

PIV incurs certain errors from statistical correlations in the interrogation areas when determining the fluid velocities. For example, consider the problem of laminar channel flow where the average fluid velocity, U, for an interrogation area at any instant is measured by the following equation:

$$U = \frac{\Delta s L_o}{\Delta t L_I} \tag{4.9}$$

where Δt is the time interval between laser pulses, Δs is the particle displacement from the correlation algorithm, L_o is the width of the camera view in the object plane, and L_I is the width of the digital image.

The total error, ε, in a measured quantity is a sum of the bias component, B, and a precision component, P. The bias error of the measured velocity is related to the elementary bias errors based on the sensitivity coefficients, that is,

$$B_u^2 = \eta_{\Delta s}^2 B_{\Delta s}^2 + \eta_{\Delta t}^2 B_{\Delta t}^2 + \eta_{Lo}^2 B_{Lo}^2 + \eta_{L_I}^2 B_{L_I}^2 \tag{4.10}$$

where the sensitivity coefficients with respect to an arbitrary variable, χ, is given by

$$\eta_\chi = \partial u / \partial \chi \tag{4.11}$$

The elementary bias limits (t, Δs) are usually specified by the manufacturer. The width of the camera view in the object plane, L_o, depends on distances and configurations related to the experimental setup, so the bias limit for L_o is determined from calibration procedures, not manufacturer's specifications. In this calibration, the physical dimensions and spatial resolution of the camera view in the measurement plane are determined. Then the width of the digital image can be determined by the number of pixels corresponding to these dimensions. The width of the camera view in the object plane and bias limit for L_o are determined. Then, the uncertainty associated with this bias limit can be reduced with a more refined procedure for measuring L_o. The PIV image pairs are cross-correlated with an interrogation window, which yields a value of Δs in the centerline. Combining the contributions of each bias error and the sensitivity coefficient, the velocity error can then be determined.

The precision error (P) of an average value, $\bar{\chi}$, measured from N samples is given by

$$P = \frac{t\sigma}{N} \tag{4.12}$$

where t is the confidence coefficient, t equals 2 for a 95% confidence level, and σ is the standard deviation of the sample of N images. The standard deviation is defined as follows:

$$\sigma = \sqrt{\frac{1}{N-1}\sum_{k=1}^{N}(\chi_k - \bar{\chi})^2} \tag{4.13}$$

where the average quantity is defined by the following equation:

$$\bar{\chi} = \frac{1}{N}\sum_{k=1}^{N}\chi_k \tag{4.14}$$

Typical values of the standard deviation along the centerline and the near-wall region of the channel can be determined from the procedure, thereby yielding the precision limits and resulting total uncertainty of the measured velocity.

4.5.3 Measurement Uncertainties of Entropy Production

Based on the previous velocity results, the errors of measured entropy production can be estimated. A data reduction equation for entropy production of laminar channel flow is approximated by

$$\dot{P}_s = \frac{\mu}{T}\left(\frac{\Delta u}{\Delta y}\right)^2 + \frac{k}{T}\left(\frac{\Delta T}{\Delta y}\right)^2 \tag{4.15}$$

The total uncertainties ($B + P$) for the U (velocity), T (temperature), and y (position) variables are

$$U_i = \bar{U}_i \pm \varepsilon_{U_i}$$
$$T_i = \bar{T}_i \pm \varepsilon_{T_i}$$
$$y_i = \bar{y}_i \pm \varepsilon_{y_i}$$

The uncertainty in ΔU is obtained as follows:

$$\varepsilon_{\Delta u} = \pm\sqrt{(\theta'_{u,i+1}\varepsilon_{u,i+1})^2 + (\theta'_{u,i-1}\varepsilon_{u,i-1})^2} \tag{4.16}$$

where

$$\theta'_{u,i-1} = \frac{\partial(\Delta u)}{\partial u_i} \tag{4.17}$$

Note that $\theta'_{u,i=-1} = -1$ and $\theta'_{u,i=-1} = 1$ or vice versa. The uncertainty of ΔT is calculated in the same manner as Equation 4.16 and Equation 4.17, except that the velocity component, U, is replaced by temperature, T. Similarly,

$$\varepsilon_{\Delta y} = \pm\sqrt{(\theta'_{y,i+1}\varepsilon_{y,i+1})^2 + (\theta'_{y,i-1}\varepsilon_{y,i-1})^2} \tag{4.18}$$

where

$$\theta'_{y,i-1} = \frac{\partial(\Delta y)}{\partial y_i} \tag{4.19}$$

Neglecting the error in reported thermophysical properties, the data reduction equation for entropy production leads to

$$\varepsilon^2_{P_s} = \eta^2_T\varepsilon^2_T + \eta^2_{\Delta u}\varepsilon^2_{\Delta u} + \eta^2_{\Delta y}\varepsilon^2_{\Delta y} + \eta^2_{\Delta T}\varepsilon^2_{\Delta T} \tag{4.20}$$

Based on this equation and the previous procedure of calculating individual uncertainties, the experimental uncertainty of entropy production can be determined. The measured uncertainties represent a maximum error bound within the 95% confidence interval.

4.5.4 Entropy Production of Free Convection in Cavities

Consider another example involving measurement uncertainties of free convection experiments described in Section 4.4. A similar procedure is adopted for the bias and precision errors. However, certain differences exist due to variations of temperature within the enclosure. Unlike the previous channel flow problem, irreversibilities in this problem vary spatially due to both velocity and temperature variations across the flow field. For this problem, the bias error of the measured velocity is related to the elementary bias errors and sensitivity coefficients as follows:

$$B_u^2 = \eta_{\Delta s}^2 B_{\Delta s}^2 + \eta_{\Delta t}^2 B_{\Delta t}^2 + \eta_{L_o}^2 B_{L_o}^2 + \eta_{L_i}^2 B_{L_i}^2 \tag{4.21}$$

where the same definition of sensitivity coefficients is used, i.e., $\eta_\chi = \partial U / \partial \chi$. By combining the contributions from each source of bias and the sensitivity coefficient, a full-scale velocity bias error is obtained. Similarly as described previously, the precision error (P) of an average value, $\overline{\chi}$, is measured from N samples. The data reduction equation for friction irreversibility of entropy production in this problem then becomes

$$P_s = \frac{\mu}{T}\left\{\left(\frac{\Delta u_y}{\Delta y}\right)^2 + \left(\frac{\Delta v_x}{\Delta x}\right)^2 + \left(\frac{\Delta u_x}{\Delta x}\right)^2 + \left(\frac{\Delta v_x}{\Delta y}\right)^2\right\} \tag{4.22}$$

The same definitions are applied from the previous problem, including the total uncertainties for the U, T, y, ΔU, and Δy variables. The total uncertainty of entropy production becomes

$$\varepsilon_{P_s}^2 = \eta_T^2 \varepsilon_T^2 + \eta_{\Delta U}^2 \varepsilon_{\Delta U}^2 + \eta_{\Delta V}^2 \varepsilon_{\Delta V}^2 + \eta_{\Delta y}^2 \varepsilon_{\Delta y}^2 \tag{4.23}$$

Then, the total uncertainty of measured entropy production can be determined. The reader is referred to past studies by Adeyinka and Naterer (1995), which provide detailed examples of measurement uncertainties of entropy production in various applications.

REFERENCES

Adeyinka, O.B. and G.F. Naterer. 2005. Particle image velocimetry based measurement of entropy production with free convection heat transfer. *ASME J. Heat Transfer,* 127(6): 615–624.

Adrian, R.J. 1991. Particle-imaging techniques for experimental fluid mechanics. *Annu. Rev. Fluid Mechanics,* 23: 261–304.

Adrian, R.J. 1997. Dynamic ranges of velocity and spatial resolution of particle image velocimetry. *Measurement Sci. Technol.,* 8: 1393–1398.

AIAA-Standard-S017-1995, Assessment of Experimental Uncertainty with Application to Wind Tunnel Testing. American Institute of Aeronautics and Astronautics. Washington, D.C.

Alekseeva, A.K. and M.I. Navon. 2002. On estimation of temperature uncertainty using the second order adjoint algorithm. *Int. J. Computational Fluid Dynamics,* 16(2): 113–117.

Alekseeva, A.K. and M.I. Navon. 2003. Calculation of uncertainty propagation using adjoint equations. *Int. J. Computational Fluid Dynamics,* 17(4): 283–288.

Coleman, H.W. and W.G. Steele. 1989. *Experimentation and Uncertainty Analysis for Engineers*. John Wiley & Sons, New York.

Coleman, H.W. and W.G. Steele. 1995. Engineering application of experimental uncertainty analysis. *AIAA J.,* 33: 1888–1896.

FlowMap Particle Image Velocimetry Instrumentation: Installation and User Guide. Dantec Dynamics, Demark, 1998.

Gui, L., Longo, J., and F. Stern. 2001. Towing tank PIV measurement system, data and uncertainty assessment for DTMB Model 5512. *Exp. Fluids,* 31: 336–346.

Kline, S.J. 1985. The purpose of uncertainty analysis. *ASME J. Fluids Eng.,* 107: 153–160.

Kline, S.J. and F.A. McClintock. 1953. Describing uncertainties in single-sample experiments. *Mechanical Eng.,* 75: 3–8.

Lassahn, G.D. 1985. Uncertainty definition. *ASME J. Fluids Eng.,* 107: 179.

Luff, J.D., Drouillard, T., Rompage, A.M., Linne, M.A., and J.R. Hertzberg. 1999. Experimental uncertainties associated with particle image velocimetry (PIV) based vorticity algorithms. *Exp. Fluids,* 26: 36–54.

Moffat, R.J. 1982. Contributions to the theory of single-sample uncertainty analysis. *ASME J. Fluids Eng.,* 104: 250–260.

Moffat, R.J. 1988. Describing the uncertainties in experimental results. *Exp. Thermal Fluid Sci.,* 1: 3–17.

Naterer, G.F. 2002. *Heat Transfer in Single and Multiphase Systems*. CRC Press, Boca Raton, FL.

Pelletier, D., Turgeon, E., Lacasse, D., and J. Borggaard. 2003. Adaptivity, sensitivity and uncertainty: Toward standards of good practice in computational fluid dynamics. *AIAA J.,* 41(10): 1925–1933.

Rosen, M.A. and I. Dincer. 2003. Exergoeconomic analysis of power plants operating on various fuels. *Appl. Thermal Eng.,* 23(6): 643–658.

Westerweel, J. 1997. Fundamentals of digital particle image velocimetry. *Measurement Sci. Technol.,* 8: 1379–1392.

Willert, C.E. and M. Gharib. 1991. Digital particle image velocimetry. *Exp. Fluids,* 10: 181–193.